

Single-protein optical holography

Received: 12 July 2023

Accepted: 13 February 2024

Published online: 13 March 2024

 Check for updatesJan Christoph Thiele ^{1,2,3}, Emanuel Pfitzner ^{1,2,3} & Philipp Kukura ^{1,2} 

Light scattering by nanoscale objects is a fundamental physical property defined by their scattering cross-section and thus polarizability. Over the past decade, a number of studies have demonstrated single-molecule sensitivity by imaging the interference between scattering from the object of interest and a reference field. This approach has enabled mass measurement of single biomolecules in solution owing to the linear scaling of image contrast with molecular polarizability. Nevertheless, all implementations so far are based on a common-path interferometer and cannot separate and independently tune the reference and scattered light fields, thereby prohibiting access to the rich toolbox available to holographic imaging. Here we demonstrate comparable sensitivity using a non-common-path geometry based on a dark-field scattering microscope, similar to a Mach–Zehnder interferometer. We separate the scattering and reference light into four parallel, inherently phase-stable detection channels, delivering a five orders of magnitude boost in sensitivity in terms of scattering cross-section over state-of-the-art holographic methods. We demonstrate the detection, resolution and mass measurement of single proteins with mass below 100 kDa. Separate amplitude and phase measurements also yield direct information on sample identity and experimental determination of the polarizability of single biomolecules.

A core challenge of optical microscopy is to generate detectable image contrast arising from micro- or nanoscopic objects and features. One of the most powerful methods in this regard relies on the phase-contrast concept originally introduced by Zernike, which paved the way towards highly sensitive imaging of phase objects. Here incident light and light scattered by an object are considered to correspond to the two arms of an interferometer, where the addition of a $\pi/2$ phase shift to the scattered light results in an amplitude modulation, which can be imaged^{1,2}. Limitations associated with this initial approach spurred the emergence of numerous variations of the original concept to enable more quantitative measurements³, as well as phase-shifting interferometry where multiple images are recorded to enable phase and amplitude imaging^{4–6}. Further developments include digital holography and quantitative phase imaging, as well as alternative implementations optimized for nanoparticle imaging, tracking and characterization^{7–10}. Regarding

sensitivity, recent advances have reached single metallic nanoparticles as small as 20 nm in imaging^{11–14} and 15 nm in differential interference measurements¹⁵. Common-path interferometry has been shown to yield holographic information as well¹⁶, although it requires recording an image sequence of the same particle, which limits the sensitivity to particles clearly visible above any static background, such as that of regularly used glass coverslips¹⁷.

Despite their unique capabilities, these efforts have struggled to match the sensitivities achieved with non-holographic, common-path interferometric approaches, which have focused on imaging and quantifying phenomena at interfaces with high sensitivity^{18,19}. The introduction of laser illumination dramatically improved the sensitivity by increasing the illumination power densities, lowering shot noise and enhancing spatiotemporal coherence of illumination. This enabled access to the nanoscale down to 5 nm gold nanoparticles (AuNPs) in

¹Kavli Institute for Nanoscience Discovery, University of Oxford, Oxford, UK. ²Physical and Theoretical Chemistry Laboratory, Department of Chemistry, University of Oxford, Oxford, UK. ³These authors contributed equally: Jan Christoph Thiele, Emanuel Pfitzner. ✉e-mail: philipp.kukura@chem.ox.ac.uk

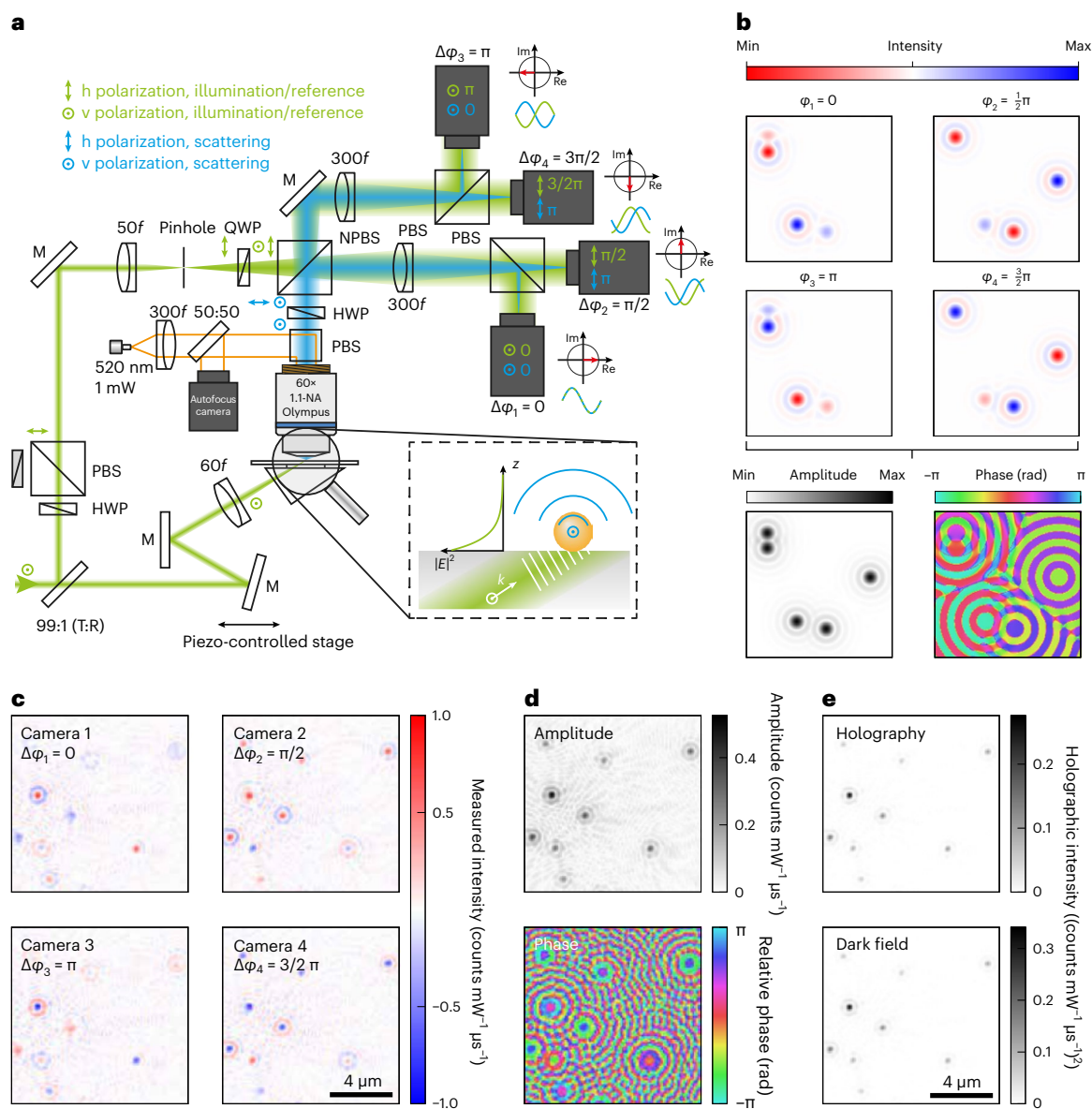


Fig. 1 | Total-internal-reflection optical quadrature microscopy. **a**, Output from a single-emitter laser diode is split by an anti-reflection-coated window. One part is focused onto an NBK7 prism to illuminate the sample. The scattered light is collected by a $\times 60$ water-dipping objective. The other part is mode filtered with a $25 \mu\text{m}$ pinhole and mixed with scattered light after introducing different phase shifts to two orthogonal polarizations. The interference of reference and scattered light is detected for each phase shift by a separate camera. Note that the PBS after the objective reflects light out of the image plane and transmits the vertical polarization. PBS, polarizing beamsplitter; NPBS, non-polarizing beamsplitter; QWP/HWP, quarter-/half-wave plate; M, mirror;

NA, numerical aperture. **b**, Illustration of an ideal measurement in the absence of substrate roughness. Depending on the phase shift, constructive or destructive interference is observed. Combining four images with the correct phase shifts reconstructs the amplitude and phase of the scattered field (bottom). Supplementary Information provides details of the calculation. **c**, Representative raw data of 40 nm AuNPs detected by the four cameras after subtraction of any non-interferometric terms. **d**, Reconstructed amplitude (top) and relative phase (bottom) of the electric field. **e**, Intensity of 40 nm AuNPs derived via holography (top) and directly derived by dark-field microscopy.

the form of interferometric scattering microscopy²⁰ and ultimately individual biomolecules^{21,22}. The latter has recently demonstrated a substantial impact on the characterization of biomolecular structures, dynamics and interactions through the development of mass photometry^{23–26}. A direct consequence of common-path imaging, however, is the difficulty to modify the reference field relative to the scattered field, causing a loss of phase information.

Here we combine sample illumination by total internal reflection with optical quadrature detection²⁷, achieving single-molecule sensitivity reported so far only for common-path approaches. In analogy to a time-domain lock-in amplifier, which mixes sinusoidal waveforms with the modulated signal, we mix four reference fields of the same colour

but different phase shifts with the scattered field to retrieve the complex amplitude of the scattered field. As a result, we measure the complex optical field of sub-diffraction particles, that is, AuNPs and single proteins. Therefore, we can experimentally quantify the polarizability of individual biomolecules, implement holography-specific capabilities such as optimizing the focus in post-processing²⁸ and demonstrate a step change in the sensitivity achievable with holographic imaging.

Results

Proof of concept

Our microscope is based on a Mach–Zehnder interferometer where a scattering object is located in one arm and the reference travels

separately along the other arm (Fig. 1a). Placing a quarter-wave plate at 45° in the reference arm generates equal amounts of vertical (v)- and horizontal (h)-polarized light with a relative phase shift of $\pi/2$. Similarly, a half-wave plate in the scattering arm at 22.5° produces equal amounts of v- and h-polarized light with a relative phase shift of π . Recombination by a non-polarizing beamsplitter (NPBS) generates four phase-shifted interferograms: two interferograms in one arm where the h and v polarizations contain phase shifts of 0 and $\pi/2$, respectively. In the other arm, the two orthogonal polarizations contain interferograms with the corresponding phase shifts of π and $3\pi/2$. The individual interferograms are then split by two polarizing beamsplitters (PBSs) and imaged onto four individual cameras, which are read synchronously.

This approach has several benefits. (1) Total-internal-reflection illumination enhances the illumination field strength at the interface and suppresses scattering from objects more than a few hundred nanometres from the interface, effectively reducing the sample-induced background. Crucially, total internal reflection almost completely extinguishes illumination light reaching the detector, except for that scattered by interface imperfections. (2) The relative amplitude of scattered and reference light can be easily adjusted to match the full-well capacity of the imaging cameras at the desired read-out speed, as well as to the expected scattering cross-sections of the sample. (3) The approach is inherently phase stable, despite a non-common-path geometry, because any phase differences identically propagate through all the channels, resulting in an excellent overall phase stability. (4) Individual blocking of either arm separately yields the reference intensity, scattering intensity and interference of both fields.

Each camera j , thus, records the interference of scattered and reference fields:

$$I_j^{\text{cam}} = |E_{\text{ref}}|^2 + |E_{\text{scat}}|^2 + 2|E_{\text{ref}}||E_{\text{scat}}|\cos(\Delta\varphi + \Delta\Phi_j), \quad (1)$$

where $\Delta\Phi_j$ is the additional phase shift introduced by the half- and quarter-wave plates in front of the NPBS. In other words, each camera records an interferogram of different phase shifts $\Delta\Phi_j \in [0, \frac{\pi}{2}, \pi, \frac{3\pi}{2}]$ (Fig. 1b), where the scattered light of each particle interferes differently with the reference field on all four cameras. To obtain the desired term $|E_{\text{scat}}|\cos(\Delta\varphi + \Delta\Phi_j)$, we subtract any non-interferometric terms from each image (reference field $|E_{\text{ref}}|^2$ and scattering field $|E_{\text{scat}}|^2$) and normalize by $|E_{\text{ref}}|$. The reference and scattered fields are directly recorded before measuring the interference of both by blocking either the scattering or the reference path. The resulting images are then combined in a complex fashion according to their phase shifts, by multiplying the corrected output of camera j by $\exp(i\Delta\Phi_j)$ and computing their average, generating the final complex-valued holographic image. The processing illustrated in Supplementary Fig. 1 restores the complex-valued scattered field E_{scat} represented by its amplitude and phase (Fig. 1b (bottom) and experimental data in Fig. 1c), which allows us to generate the respective amplitude and relative phase images (Fig. 1d). Due to the unknown illumination phase, we only obtain a relative phase and not an absolute one. Reassuringly, the scattered intensity derived via the square of the holographically reconstructed scattered field $|E_{\text{scat}}^{\text{holo}}|^2$ is identical in both appearance and intensity to the dark-field intensity $|E_{\text{scat}}^{\text{DF}}|^2$ of the same field of view recorded with identical acquisition parameters by blocking the reference arm (Fig. 1e). These results demonstrate that our approach indeed accurately extracts the scattering amplitude, with a deviation of only ~20% probably stemming from imperfect coherence between the reference and scattered fields. This constant scaling can be compensated with a calibration if absolute values for the scattered field are desired. With a laser coherence length of approximately $150 \mu\text{m}$ (Supplementary Fig. 2), we ensure a consistent degree of interference over the field of view and avoid background interference from additional reflections. We normalized all data to exposure time and laser power to ensure comparability between different experimental settings.

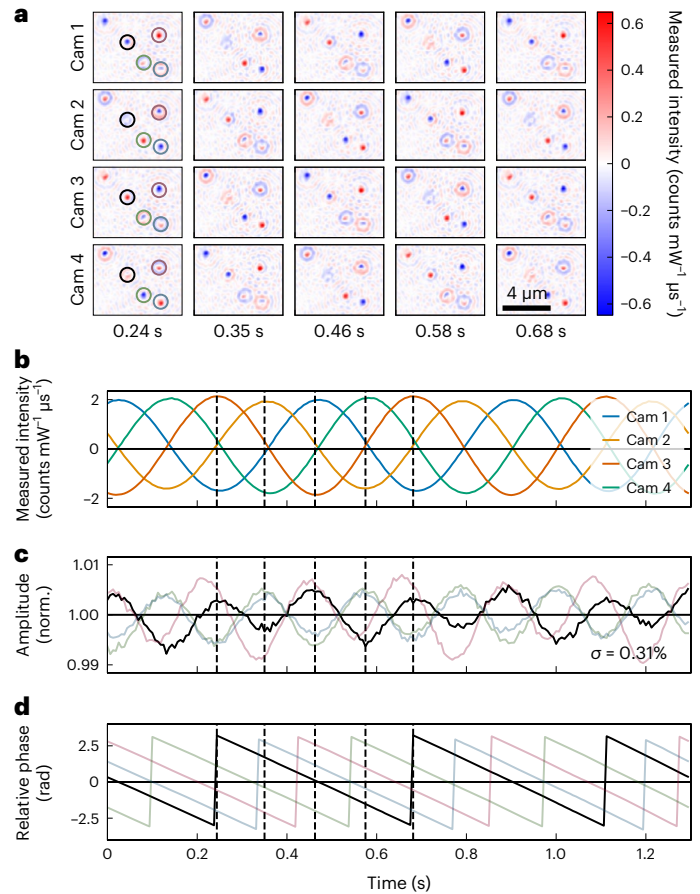


Fig. 2 | Holography of 40 nm AuNPs and resulting amplitude and phase decoupling. **a**, Images of four cameras (phase shifts $0, \pi/2, \pi$ and $3\pi/2$) with different phase shifts introduced by a movable mirror in the illumination arm. **b**, Temporal evolution of the detected interference of a single AuNP (black circle in **a**). Each trace corresponds to a different camera. **c, d**, Reconstructed amplitude (**c**) and relative phase (**d**). The black trace corresponds to the highlighted AuNP and the lighter-coloured ones, to the other particles in the field of view. The black amplitude trace has a relative standard deviation of 0.31%.

Demonstration of amplitude and phase decoupling

Having verified that we can retrieve the correct scattering intensity, we turn to the accuracy of our amplitude and phase measurements. To achieve this, we record videos where we temporally vary the phase between the scattering and reference arms in a linear fashion by a piezo-driven mirror in the scattering/illumination arm (Fig. 1a). The intensity of individual particles as a function of time reveals clear oscillatory behaviour (Fig. 2a,b). This is caused by the interference between the scattered field of each particle and the reference, which exhibits a constant phase shift $\Delta\Phi_j$ and an additional temporally modulated phase shift, resulting in a global phase shift $\Delta\varphi(t)$ between the fields. Following the intensity of a particular particle (Fig. 2a, black circle) on all four cameras reveals sinusoidal modulations shifted by $\frac{\pi}{2}, \pi$ and $\frac{3\pi}{2}$ relative to the first camera (blue trace). Despite the fact that the intensity in the individual camera images varies by $\pm 100\%$, the reconstruction of the complex-valued scattered field yields a constant amplitude with a standard deviation of only 0.31%, demonstrating excellent separation of phase and amplitude. A residual variation in the amplitude might be related to imperfect circular and linear polarization states generated by the quarter- and half-wave plates, respectively, leading to phase shifts between the scattered and reference fields deviating slightly from multiples of $\frac{\pi}{2}$ (Supplementary Fig. 3). The phase ramps down linearly as introduced by the movable mirror. The same behaviour can be observed for all the other

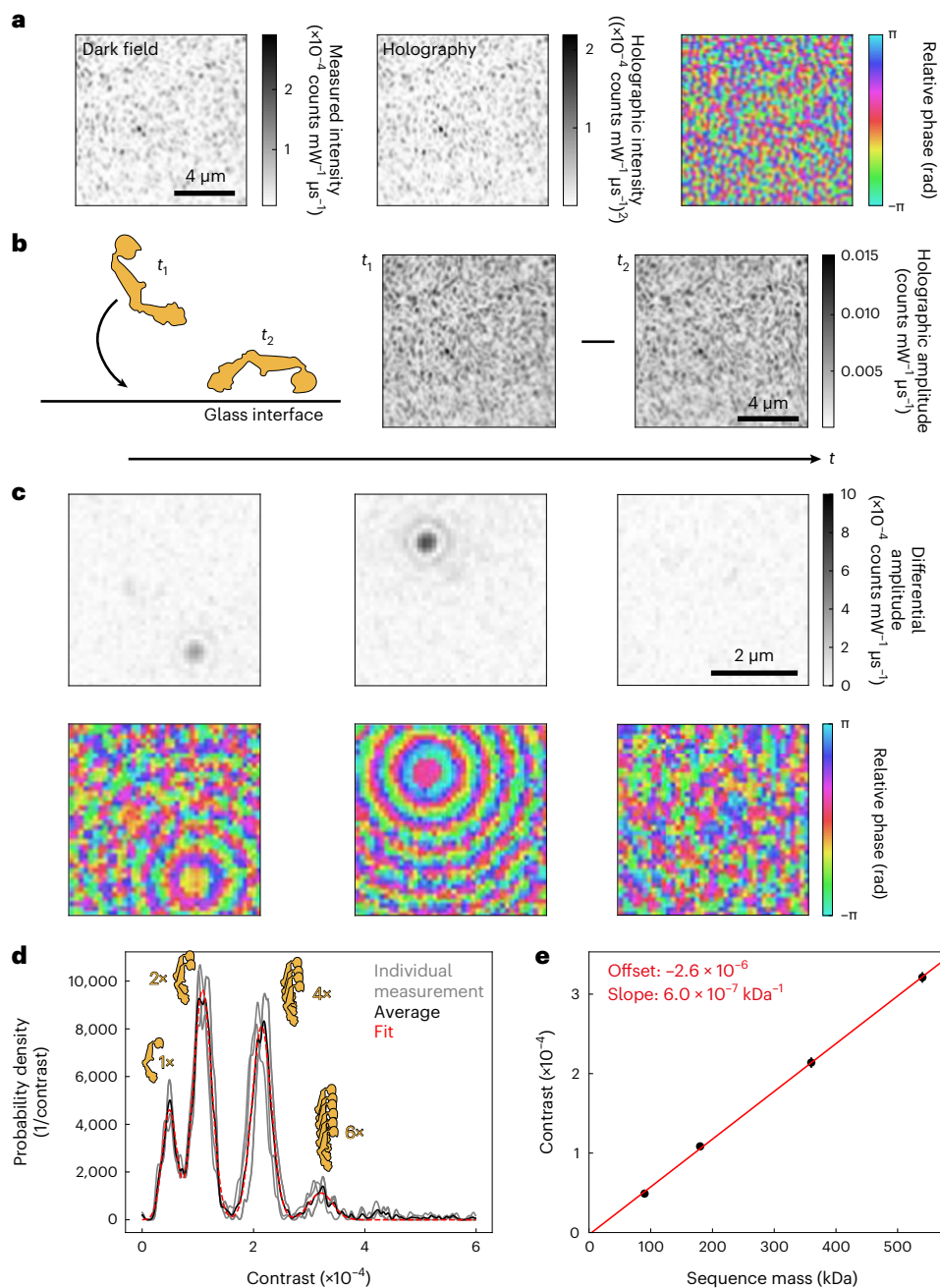


Fig. 3 | Single-protein holography. **a**, Dark-field and holographically reconstructed intensity and phase maps of a microscope coverslip exhibiting typical residual glass roughness. **b**, Amplitude image of the glass surface does not visibly change before and after a single protein landed. **c**, Moving mean differences of subsequent image stacks reveal individual proteins landing in the amplitude and phase representations. **d**, Amplitude histograms (grey)

of the landing events from individual videos acquired over 120 s. The red line represents a fit of four Gaussians to the averaged data shown in black. **e**, Fitted contrast versus sequence mass of the different oligomers. The red line indicates a linear fit to the data points. The error bars give the standard error across three measurements and are in the order of the data point size.

particles in the region of interest (Fig. 2c,d, light traces). Additional measurements without phase ramping (Supplementary Fig. 4) confirm the high overall phase stability with a fluctuation of only a few milliradians per second.

Optical holography of individual proteins

Given these encouraging results, we queried to which degree this approach may be suited to detect, image and quantify very weak scatterers, such as individual proteins. A cleaned microscope glass coverslip produces a speckle pattern (Fig. 3a) reminiscent of that observed in iSCAT²⁹ and high-performance dark-field microscopy³⁰.

Again, the dark-field and holographically reconstructed images show excellent quantitative agreement. Introducing ~ 40 nM of a soluble 90 kDa protein (Dyn Δ PRD) results in no discernible changes to the amplitude images as a function of time (Fig. 3b). Computing the differences of the mean of two moving subsequent windows with a length of ten frames (6.25 ms per frame), however, reveals clear signatures of individual proteins binding to the surface in both amplitude and phase (Fig. 3c). We then quantified the contrast of each landed protein by fitting a complex-valued point spread function (PSF) model derived from the average PSF of all the landing events (Fig. 3d and Methods).

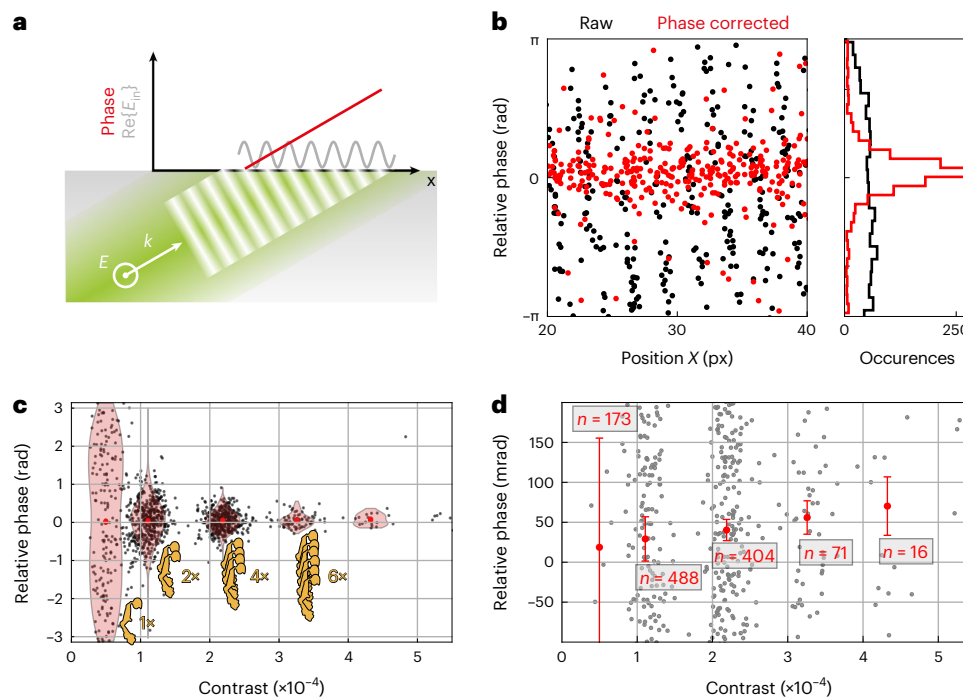


Fig. 4 | Phase-sensitive microscopy of single-proteins. **a**, Oblique angle of illumination imprints a phase gradient onto the scattered light as a function of landing position. **b**, Phase values of landing events versus landing position (black data points). The subtraction of a linear phase gradient removes the spatial dependence of the phase (red data points). **c**, Relative phase of each

landing event versus its contrast. The red areas depict a Gaussian kernel density estimation of the data via violin plots. Each violin plot was separately generated for each oligomer. **d**, Zoomed-in view of the data shown in **c**. The grey data points are the raw data, whereas red represents the average of each oligomeric distribution together with its standard error.

The resulting histogram exhibits several sub-distributions, corresponding to the monomer, dimer, tetramer and hexamer of dynamin (DynΔPRD), as reported recently²⁵. Their fitted masses correlate well with the expected molecular weights of 90, 180, 360 and 540 kDa (Fig. 3e). The linear relationship between contrast and molecular weight allows us to deduce the mass of any unknown protein based on its image contrast, with an average mass resolution of 28 kDa. Although this mass resolution is slightly higher compared with state-of-the-art mass photometry²⁴, we expect substantial improvements achievable by optimizing the illumination power and geometry.

In principle, we could also derive the scattering intensity by collecting the dark-field scattering (Fig. 1e). Supplementary Fig. 5 shows the PSF and histogram of protein landing events at the same glass spot generated via holography and synthetic dark field. It is apparent that only the interferometric approach yields well-defined events, whereas the PSFs are distorted for dark-field imaging. As explained in the Supplementary Information, in dark-field operation, the scattered field interferes with the complicated wavefront of light scattered by the glass interface, which prevents an accurate contrast estimate.

Until now, we only investigated the amplitude of landing events. However, we simultaneously derive the phase shift associated with each event. The oblique illumination associated with total internal reflection imprints a linear phase gradient onto the illumination field (Fig. 4a). This gradient is corrected (Fig. 4b) by subtracting a position-dependent phase from each landing event (Supplementary Information).

The corrected phase of all the individual oligomeric species falls onto a line, as expected for a non-absorbing dielectric nanoparticle (Fig. 4c)¹². As confirmed by the simulation (Supplementary Fig. 8), the corrected phase becomes less well defined as the contrast of the particle becomes lower, due to decreasing localization precision. Note that we are not able to derive the absolute phase of the landing particles as we lack knowledge about the phase relation between the illumination and reference fields. Zooming into the data along the phase axis

(Fig. 4d) reveals a slight but steady increase in the relative phase with increasing contrast. This is to be expected, since the centre of mass of heavier and thus larger particles will be further separated from the interface compared with lighter particles. Furthermore, knowledge of the complex scattered field enables us to change the focus during data analysis (Supplementary Fig. 9a,b and Supplementary Information)³¹. The standard deviation derived from the differential amplitude data correlates well with the contrast to mass conversion (Supplementary Fig. 9c). We exploit this to automatically optimize the focus for all our measurements to maximize the imaging contrast in post-processing.

Measurement of the polarizability of a single protein

Our holographic approach independently quantifies the scattered field of any unknown phase and optimizes focusing during post-processing, both for AuNPs and dielectric proteins. We use these capabilities to derive an experimental estimate for the polarizability of a protein attached to a glass coverslip per molecular weight, which we will call the specific polarizability. As a calibration, we first measure the contrast of static AuNPs of different diameters (20, 40 and 60 nm), because their polarizability is well understood and characterized. The contrast is normalized to exposure time and laser power, which we reduced for the larger AuNPs (40 and 60 nm). We did not use smaller AuNPs to ensure clear visibility above the coverglass background.

As long as Rayleigh scattering dominates, the holographic contrast depends on $|E_{\text{scat}}| \propto \alpha \propto V \propto r^3$, whereas the dark-field contrast is described by $|E_{\text{scat}}|^2 \propto \alpha^2 \propto V^2 \propto r^6$. Therefore, plotting the third root of the holographic data (Fig. 5a) and sixth root of the dark-field data (Fig. 5b) linearizes the values with respect to the particle radius r . The linear scaling of the mean values of $c^{1/3}$ and $c^{1/6}$, respectively, again indicates the agreement of the retrieved scattering amplitude with theoretical predictions. The values gathered via dark-field microscopy are 20% (in intensity) and 3% (in intensity)^{1/6} larger than the values retrieved by holography, consistent with imperfect coherence (Fig. 1e).

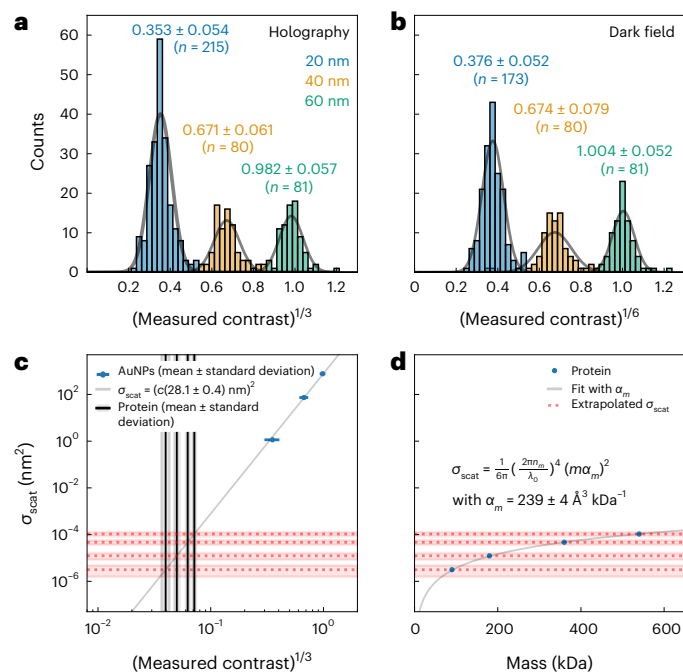


Fig. 5 | Quantification of the polarizability of a single protein. **a, b**, Histogram of the third root of the holographically derived particle contrast (**a**) and sixth root of particle contrast derived from dark-field images for 20, 40 and 60 nm AuNPs (**b**). **c**, Calibration of the scattering cross-section using AuNPs. The blue data points are the holographically derived contrasts (**a**) versus their scattering cross-section calculated using Mie theory. The grey line is a one-parameter linear fit to the sixth root of the scattering cross-section. The black lines indicate the measured contrast of our oligomeric protein sample. **d**, Based on the calibration in **c**, we can plot the scattering cross-section of proteins (red dashed lines) versus their theoretical molecular weight (blue data points). The solid line represents a fit of equation (2) to the data.

For each particle size, we calculate a scattering cross-section (Fig. 5c) by assuming the AuNPs to be homogeneous and embedded in a homogeneous medium of refractive index $n = 1.337$. As previously shown³², the scattering cross-section of the AuNPs used here (ranging from 20 to 60 nm) can be well estimated by Mie scattering. By performing a one-parameter linear regression on the derived scattering cross-section against our measured contrast, we estimate the scattering cross-section of the measured protein, assuming equal collection efficiency and near-field enhancement in total-internal-reflection illumination³³ for AuNPs and proteins (Fig. 5d). We assume the scattering of the protein to be well described by the Rayleigh scattering of a dielectric particle³⁴:

$$\sigma_{\text{scat}} = \frac{1}{6\pi} \left(\frac{2\pi n_m}{\lambda_0} \right)^4 \alpha^2. \quad (2)$$

Fitting the scattering cross-section of the protein to equation (2) yields a specific excess polarizability α per molecular weight of $239 \pm 4 \text{ \AA}^3 \text{ kDa}^{-1}$. The statistical error is propagated from the standard deviations of the fit parameters. Assuming a specific volume of 0.7446 ml g^{-1} (refs. 24,35), we can estimate the refractive index of the protein to $n = 1.47$. Both these values—specific polarizability and refractive index—are well within the range of values reported previously in the literature^{36–38}, although somewhat smaller than that recently calculated using an atomic polarizability model³⁹. We remark that this polarizability measurement by comparison with AuNPs is distinct to similar efforts made with a common-path geometry, like iSCAT or mass photometry, because they only yield an intensity, convolving amplitude and phase contributions, with the phase generally being ill-defined. This is a consequence of the Gouy phase contribution of both scattered

and reflected light, which is difficult to accurately quantify when performing experiments with single-molecule sensitivity. Furthermore, a precise evaluation of the scattered phase shift for nanoparticles $>30 \text{ nm}$ is non-trivial due to contributions from path-length variations and scattering phase.

Discussion

Using an inherently phase-stable approach, we have demonstrated holographic imaging with a sensitivity reaching single biomolecules with an average mass resolution of 28 kDa and a dynamic range beyond 10^3 in terms of holographic contrast. Although the approach was currently unable to match the sensitivity and measurement precision achievable with mass photometry, there are clear routes to potential future improvements. First, our current experimental arrangement was limited to a power density of 50 kW cm^{-2} , an order of magnitude lower than in mass photometry, resulting in a loss of shot-noise-limited sensitivity. Additionally, we did not yet optimize the electric-field enhancement due to field confinement through total internal reflection as a function of incidence angle, resulting in a relatively low 10% enhancement compared with the in-principle-achievable factor of three in intensity³³.

This confinement-induced increase in incident intensity at the detection interface will increase sample scattering for a constant power entering the sample. In addition, we expect a reduction in background scattering arising from a non-penetrating field, improvement in contrast through the ability to optimize the phase difference between scattered and reference light, reduction in image noise due to a lack of beam scanning and shot noise background optimization by matching the image intensity to camera capabilities. Furthermore, the illumination phase gradient has the potential to reduce coherent background by distribution over all the channels. Illumination with a rapidly scanned standing wave together with active phase modulation, similar to structured illumination microscopy⁴⁰ or modulated localization microscopy⁴¹, would enable a constant-illumination phase and therefore eliminate the current phase uncertainty caused by limited localization precision. Additionally, a bleed-through channel via the scattering arm would enable the measurements of the absolute scattering phase. This could be realized by immobilizing dielectric nanoparticles that would offer precise control over the density and scattering strength. We expect that these future improvements have the potential to deliver sensitivity and mass resolution of single-molecule mass measurement beyond those achievable with far-field, common-path geometries. Furthermore, the use of a prism as a sample substrate provides an avenue towards the realistic use of atomically flat substrates, which would reduce or even eliminate optical background and associated mass broadening.

Taken together, we have presented an implementation of optical quadrature microscopy in combination with total-internal-reflection illumination capable of holographic imaging of single biomolecules. We verified our approach by showcasing the ability to separate the amplitude and phase of the scattered field and confirmed its quantification by a direct comparison with dark-field microscopy. The resulting sensitivity enables the imaging of individual biomolecules, which can be converted into a measurement of the polarizability of a single protein based on the scattering of a well-characterized reference object. These results break new ground for optical holography, providing access to the exciting sub-20 nm length scale for phase and amplitude imaging with applications in the biological, physical and materials sciences. Among others, our method will enable the detailed optical characterization of quantum and carbon dots, differentiation of AuNPs with different shapes and distance measurements of single particles and proteins on the nanometre scale.

Online content

Any methods, additional references, Nature Portfolio reporting summaries, source data, extended data, supplementary information,

acknowledgements, peer review information; details of author contributions and competing interests; and statements of data and code availability are available at <https://doi.org/10.1038/s41566-024-01405-2>.

References

- Zernike, F. Phase contrast, a new method for the microscopic observation of transparent objects. *Physica* **9**, 686–698 (1942).
- Zernike, F. Phase contrast, a new method for the microscopic observation of transparent objects part II. *Physica* **9**, 974–986 (1942).
- Allen, R. D., David, G. B. & Nomarski, G. The Zeiss-Nomarski differential interference equipment for transmitted-light microscopy. *Z. Wiss. Mikrosk.* **69**, 193–221 (1969).
- Bruning, J. H. et al. Digital wavefront measuring interferometer for testing optical surfaces and lenses. *Appl. Opt.* **13**, 2693–2703 (1974).
- Lai, G. & Yatagai, T. Generalized phase-shifting interferometry. *J. Opt. Soc. Am. A* **8**, 822–827 (1991).
- Hettwer, A., Kranz, J. & Schwider, J. Three channel phase-shifting interferometer using polarization-optics and a diffraction grating. *Opt. Eng.* **39**, 960–966 (2000).
- Nguyen, T. L. et al. Quantitative phase imaging: recent advances and expanding potential in biomedicine. *ACS Nano* **16**, 11516–11544 (2022).
- Verpillat, F., Joud, F., Desbiolles, P. & Gross, M. Dark-field digital holographic microscopy for 3D-tracking of gold nanoparticles. *Opt. Express* **19**, 26044–26055 (2011).
- Midtvedt, D. et al. Size and refractive index determination of subwavelength particles and air bubbles by holographic nanoparticle tracking analysis. *Anal. Chem.* **92**, 1908–1915 (2020).
- Hauler, O. et al. Direct phase mapping of the light scattered by single plasmonic nanoparticles. *Nanoscale* **12**, 1083–1090 (2020).
- Goto, K. & Hayasaki, Y. Three-dimensional motion detection of a 20-nm gold nanoparticle using twilight-field digital holography with coherence regulation. *Opt. Lett.* **40**, 3344–3347 (2015).
- Saemisch, L., van Hulst, N. F. & Liebel, M. One-shot phase image distinction of plasmonic and dielectric nanoparticles. *Nano Lett.* **21**, 4021–4028 (2021).
- Ortiz-Orruno, U., Jo, A., Lee, H., van Hulst, N. F. & Liebel, M. Precise nanosizing with high dynamic range holography. *Nano Lett.* **21**, 317–322 (2021).
- Ortiz-Orruno, U., Quidant, R., van Hulst, N. F., Liebel, M. & Ortega Arroyo, J. Simultaneous sizing and refractive index analysis of heterogeneous nanoparticle suspensions. *ACS Nano* **17**, 221–229 (2023).
- Stoller, P., Jacobsen, V. & Sandoghdar, V. Measurement of the complex dielectric constant of a single gold nanoparticle. *Opt. Lett.* **31**, 2474–2476 (2006).
- Lee, H., Park, H., Yeon, G. J. & Kim, Z. H. Amplitude and phase spectra of light scattered from a single nanoparticle. *ACS Photonics* **9**, 3052–3059 (2022).
- Lee, I. B. et al. Interferometric scattering microscopy with polarization-selective dual detection scheme: capturing the orientational information of anisotropic nanometric objects. *ACS Photonics* **5**, 797–804 (2018).
- Curtis, A. S. G. The mechanism of adhesion of cells to glass. *J. Cell Biol.* **20**, 199–215 (1964).
- Limozin, L. & Sengupta, K. Quantitative reflection interference contrast microscopy (RICM) in soft matter and cell adhesion. *ChemPhysChem* **10**, 2752–2768 (2009).
- Lindfors, K., Kalkbrenner, T., Stoller, P. & Sandoghdar, V. Detection and spectroscopy of gold nanoparticles using supercontinuum white light confocal microscopy. *Phys. Rev. Lett.* **93**, 037401 (2004).
- Ortega Arroyo, J. et al. Label-free, all-optical detection, imaging, and tracking of a single protein. *Nano Lett.* **14**, 2065–2070 (2014).
- Piliarik, M. & Sandoghdar, V. Direct optical sensing of single unlabelled proteins and super-resolution imaging of their binding sites. *Nat. Commun.* **5**, 4495 (2014).
- Cole, D., Young, G., Weigel, A., Sebesta, A. & Kukura, P. Label-free single-molecule imaging with numerical-aperture-shaped interferometric scattering microscopy. *ACS Photonics* **4**, 211–216 (2017).
- Young, G. et al. Quantitative mass imaging of single biological macromolecules. *Science* **360**, 423–427 (2018).
- Foley, E. D. B., Kushwah, M. S., Young, G. & Kukura, P. Mass photometry enables label-free tracking and mass measurement of single proteins on lipid bilayers. *Nat. Methods* **18**, 1247–1252 (2021).
- Liebel, M., Hugall, J. T. & van Hulst, N. F. Ultrasensitive label-free nanosensing and high-speed tracking of single proteins. *Nano Lett.* **17**, 1277–1281 (2017).
- Hogenboom, D. O., DiMarzio, C. A., Gaudette, T. J., Devaney, A. J. & Lindberg, S. C. Three-dimensional images generated by quadrature interferometry. *Opt. Lett.* **23**, 783 (1998).
- Dubois, F., Schockaert, C., Callens, N. & Yourassowsky, C. Focus plane detection criteria in digital holography microscopy by amplitude analysis. *Opt. Express* **14**, 5895–5908 (2006).
- Lin, S., He, Y., Feng, D., Piliarik, M. & Chen, X. W. Optical fingerprint of flat substrate surface and marker-free lateral displacement detection with angstrom-level precision. *Phys. Rev. Lett.* **129**, 213201 (2022).
- Weigel, A., Sebesta, A. & Kukura, P. Dark field microspectroscopy with single molecule fluorescence sensitivity. *ACS Photonics* **1**, 848–856 (2014).
- Shen, F. & Wang, A. Fast-Fourier-transform based numerical integration method for the Rayleigh-Sommerfeld diffraction formula. *Appl. Opt.* **45**, 1102–1110 (2006).
- Ortiz-Orruno, U., Jo, A., Lee, H., van Hulst, N. F. & Liebel, M. Precise nanosizing with high dynamic range holography. *Nano Lett.* **21**, 317–322 (2020).
- Carniglia, C. K., Mandel, L. & Drexhage, K. H. Absorption and emission of evanescent photons*. *J. Opt. Soc. Am.* **62**, 479–486 (1972).
- Bohren, C. F. & Huffman, D. R. *Absorption and Scattering of Light by Small Particles* (Wiley, 1983).
- Harpaz, Y., Gerstein, M. & Chothia, C. Volume changes on protein folding. *Structure* **2**, 641–649 (1994).
- Špačková, B. et al. Label-free nanofluidic scattering microscopy of size and mass of single diffusing molecules and nanoparticles. *Nat. Methods* **19**, 751–758 (2022).
- Scarangella, A. et al. Adsorption properties of BSA and DsRed proteins deposited on thin SiO₂ layers: optically non-absorbing versus absorbing proteins. *Nanotechnology* **29**, 115101 (2018).
- Guemouri, L., Ogier, J. & Ramsden, J. J. Optical properties of protein monolayers during assembly. *J. Chem. Phys.* **109**, 3265–3268 (1998).
- Becker, J. et al. A quantitative description for optical mass measurement of single biomolecules. *ACS Photonics* **10**, 2699–2710 (2023).
- Heintzmann, R. & Huser, T. Super-resolution structured illumination microscopy. *Chem. Rev.* **117**, 13890–13908 (2017).
- Jouchet, P. et al. Nanometric axial localization of single fluorescent molecules with modulated excitation. *Nat. Photon.* **15**, 297–304 (2021).

Publisher's note Springer Nature remains neutral with regard to jurisdictional claims in published maps and institutional affiliations.

Open Access This article is licensed under a Creative Commons Attribution 4.0 International License, which permits use, sharing, adaptation, distribution and reproduction in any medium or format, as long as you give appropriate credit to the original author(s) and the source, provide a link to the Creative Commons licence, and indicate if changes were made. The images or other third party material in this

article are included in the article's Creative Commons licence, unless indicated otherwise in a credit line to the material. If material is not included in the article's Creative Commons licence and your intended use is not permitted by statutory regulation or exceeds the permitted use, you will need to obtain permission directly from the copyright holder. To view a copy of this licence, visit <http://creativecommons.org/licenses/by/4.0/>.

© The Author(s) 2024

Methods

Setup

The optical setup used in this study is similar to previously reported optical quadrature microscopes^{27,42}. A schematic of the setup is shown in Fig. 1a and Supplementary Fig. 10 shows a photograph. A single-emitter laser diode (450 nm, 500 mW, NDB4816, Nichia) is mounted in a temperature-controlled mount (Thorlabs, 400 mA, 17 °C) and collimated using an aspheric lens ($f = 3.30$ mm, N414TM-A, Thorlabs). The polarization is vertically aligned using the light reflected off a PBS (PBS251, Thorlabs) and guided to an anti-reflection-coated NBK7 window (WW11050-A, Thorlabs), which picks up $\sim 0.5\%$ of incident power and reflects it into the reference arm. More than 99% of light propagates towards the prism (12.7 mm Littrow prism (90-60-30), Edmund Optics) and is focused into the focal plane of the objective using an achromatic lens ($f = 60$ mm, AC254-60-A, Thorlabs). Standard glass coverslips (24×75 mm²; thickness, 1.5; Carl Roth) are optically coupled to the prism by immersion oil ($n = 1.52$) to enable the fast exchange of samples without the need for cleaning the prism. Scattered light from the coverslip surface is collected using an objective ($\times 60$, 1.1 numerical aperture, water dipping, Olympus) and is imaged onto four different cameras by an achromatic tube lens ($f = 300$ mm, AC254-300-A, Thorlabs). It is important to note that the tube lens is placed one focal length away from the back focal plane of the objective to create a flat wavefront in the image plane. The light reflected towards the reference arm is focused by an achromatic lens ($f = 50$ mm, AC254-50-A, Thorlabs) onto a 25 μm pinhole (P25CB, Thorlabs) to filter the mode of the laser. The diverging light is then collimated by the tube lens.

The central elements of this optical scheme are the two wave plates in front of the NPBS: the two orthogonal polarizations of the reference arm are phase shifted by a quartz quarter-wave plate (WPQ05M-445, Thorlabs), resulting in a phase shift of 0 and $\pi/2$ for h and v polarizations, respectively. External reflection off the NPBS introduces an additional phase shift of π , whereas the transmitted polarizations are not affected. Light coming from the scattering arm propagates through the polymer half-wave plate (WPH05ME-445, Thorlabs), which introduces 0 and π phase shifts to the two orthogonal polarizations. Mixing the reference and scattering light at the NPBS and separating them via a PBS allows to create an image with the relative phase shifts of 0, $\pi/2$, π and $3\pi/2$. The four cameras (Grasshopper GS3-U3-23S6M-C, Teledyne FLIR) detect the four phase-shifted images at 800 frames per second in a synchronized fashion. Five consecutive frames are averaged, and the data from all the cameras are aligned to the first camera (affine transformation: scale, shift, rotation) followed by a 2.0×2.0 px² binning, resulting in an effective pixel size of 117.2 nm.

To find and maintain focus in all the measurements, a collimated laser beam (0.5 mW, 520 nm, Thorlabs) propagates through the back aperture of the objective. The light is focused onto the coverslip–buffer interface. The reflected light is collimated and imaged by a camera through a 50/50 NPBS. The radius of the resulting circle is maintained by a proportional–integral–derivative controller that controls the axial distance between the objective and coverslip. All data acquisition and control is handled by a custom-built LabVIEW (LabVIEW 2018 SP1, National Instruments) program.

To achieve a phase-stable interferometer, we considered the following details as critical. (1) The beam path was chosen to be as low as 52 mm to minimize thermal drifts and mechanical vibrations. (2) All the core components of the interferometer (except the sample stage) were interconnected with a 30 mm cage system to further minimize the relative motion of optical components over time. (3) Where possible, the beam path was covered with plastic covers clipped into the rods of the cage system (C30L24, Thorlabs) to minimize air density fluctuations. (4) A separate cover was placed to house the whole microscope to further minimize air density fluctuations. (5) The temperature of the laser diode mount was equilibrated after switching on the emission for at least 30 min.

AuNP samples

All AuNPs were purchased from NanoPartz (A11-20-CIT-DIH-1-10, A11-40-CIT-DIH-1-10 and A11-60-CIT-DIH-1-10). First, clean coverslips were rendered hydrophilic by placing them in an O₂ plasma for 30 s (30% power, 0.5 mbar O₂, Zepto-BRS 200, Diener electronic). For all sizes of AuNPs, 10 μl was spin coated onto the hydrophilic coverslips for 18 s at 500 r.p.m. and 18 s and 60 s at 1,400 r.p.m. A polydimethylsiloxane gasket (CultureWell CW-8R-1.0, Grace Bio-Labs) was placed at the centre of the coverslip and 50 μl MilliQ water was added to achieve immersion with the objective lens.

Protein landing assay

Dyn Δ PRD²⁵ was diluted 25–50 fold from its stock concentration to 80–40 nM before replacing the droplet for immersion with the diluted solution. Landing events were recorded for 2 min after replacing the immersion solution.

Data analysis

All the analysis was performed in custom Python scripts⁴³. Raw data were first aligned by finding an affine transform, which minimizes the least squares of the differences of the aligned and target images. We used only the scattered intensity for aligning the four channels since it showed higher contrast than the interferometric measurement and resulted in a more reliable alignment. The data were then pixel binned (2×2 binning) and normalized to the exposure time and laser power. To extract the complex scattered field of static images, first the reference image and dark field (both recorded shortly before acquiring the holographic data) were subtracted. To extract the scattered field only, the resulting image was divided by the square root of the reference image. The resulting image now only contains $2|E_{\text{scat}}|\cos(\Phi)$ projected along the positive and negative real and imaginary axes of a complex plane. By averaging the four images rotated all onto the positive real axis, the complex field E_{scat} is recovered.

For static measurements, particles were detected on the absolute of the reconstructed scattering field $|E_{\text{scat}}|$ by calculating a radial symmetry map ($\alpha = 1.0$, radius = 3 px)⁴⁴ and finding the local maxima with radial symmetry above the 99% quantile of the map.

Fitting static particles with the analytic PSF model

For fitting the scattered field of particles, the following complex-valued PSF model was used:

$$E(r, \varphi) = |E_0| \left(\frac{2J_1\left(\frac{r}{\sigma}\right)}{\frac{r}{\sigma}} \exp(i\varphi) \right), \quad (3)$$

where J_1 denotes the Bessel function of the first kind; σ , the width; r , the distance from the centre; $|E_0|$, the amplitude; and φ , the phase of the landing event. The squared residuals (SR) of the sum of the real and imaginary parts of the PSFs were used as an objective function for minimization by optimizing x , y , $|E_0|$ and φ :

$$\text{SR} = \text{Re}\{\text{data} - E(x, y)\}^2 + \text{Im}\{\text{data} - E(x, y)\}^2. \quad (4)$$

For the data presented in Figs. 2c,d and 5a, the measurements of immobilized nanoparticles were analysed during which the length of the sample path was varied with a piezo-shifted mirror to introduce a phase shift. A segment of the measurement where the phase shift linearly increased by 6π was selected; the particles were detected on a sum of $|E_{\text{scat}}|$ over all the phase shifts. A 23×23 px² thumbnail was independently fitted with the complex PSF for each phase shift. For Fig. 5a, the cubic roots of the amplitudes were averaged over all the phase shifts and particles, with a relative standard deviation of the cubic root of the amplitude above 10% or a standard deviation of the position above 0.2 px was rejected.

The dark-field measurements of immobilized nanoparticles were analysed in a similar way. For the particle fitting, the scattered intensity $|E_{\text{scat}}|^2$ was independently fitted with an intensity PSF (square of the complex PSF in equation (3)) in all the four channels. For Fig. 5b, the sixth roots of the amplitudes were averaged over all the channels and particles, with a relative standard deviation of the sixth root of the amplitude above 10% or a standard deviation of the position above 0.2 px was rejected.

For dynamic videos (that is, landing events of proteins), only the reference image was subtracted. The resulting image was divided by the square root of the reference and the complex video was calculated by complex summation (Fig. 1). Temporal phase changes were corrected by applying the phase shift θ_{corr} , which minimizes the difference to the first frame.

$$\min_{\theta_{\text{corr}}} (||E_{\text{scat}}(t) - |E_{\text{scat}}(t=0)||) \quad (5)$$

The corrected complex video was then further analysed by a sliding difference of ten-frame window length to remove static features like the glass roughness and other proteins that landed before the analysed window. As shown in Supplementary Fig. 11, the phase correction reduces the noise in the differential images.

Detection and fitting of protein landing events

For detecting the position and time of the landing events, a normalized cross-correlation with a complex PSF (equation (3)) was applied to the video followed by a maximum filter. The resulting mask was then multiplied by the previous normalized cross-correlation and thresholded at 0.15. This essentially gives the first approximation of the location and time of all the landing events. We then convolved the mask with a circle of radius 2 along the spatial axes and a pulse function along the temporal axis with a length of ten frames to blur the found particle locations. We then searched for the local maximum of the scattering amplitude in this mask, which we define as the landing position and time.

Next, we created an experimental PSF model from the found events to compensate for potential aberrations. First, a 23×23 px² thumbnail at the detected landing event position was fitted by the complex PSF model (equation (3)), as described above, to find the refined spatial coordinates for all the determined landing events. Coordinates that deviated by more than 1 px from their initial guess were discarded to suppress outliers from entering the experimental PSF model. Then, 23×23 px² thumbnails at the refined and filtered positions were averaged in a complex manner, generating an average PSF. The average PSF was then interpolated to create a complex-valued experimental PSF model, which we used to fit the individual thumbnails found at the refined positions minimizing the SR as described above (equation (4)). The events contributing to the histogram were filtered according to position precision (fit position closer than 1 px to the initial guess), fit position (omit events too close to the border and trim events where the illumination intensity is too uneven) and fit residuals (Supplementary Fig. 12).

Calculation of protein polarizability

The scattering cross-section of the AuNPs was calculated with the Mie formalism⁴⁵ for a wavelength of 450 nm and a refractive index of $n_{\text{Au}} = 1.528 + 1.911i$ for gold⁴⁶ and 1.337 for the embedding medium (H₂O) (ref. 47). The linear scaling factor between the cubic root of the interferometric contrast c of the single particles and the sixth root of the scattering cross-section σ_{scat} was determined with an ordinary least squares⁴⁸ $\sigma_{\text{scat}} = (c \times (28.1 \pm 0.4) \text{ nm})^2$. By using the cubic root of the interferometric contrast, a normal distribution in particle diameter is assumed instead of a normal distribution in volume. With this relation, the scattering cross-section of the different protein oligomers (Fig. 5d) is estimated. From the Gaussian fits to the contrast

distributions of the oligomers and their known masses m , the relationship $c = m(6.82 \pm 0.04) \times 10^{-7} \text{ kDa}^{-1}$ was determined with a least squares regression using the inverse of the fitted peak variance as respective weights. Combining these two relationships with the formula for Rayleigh scattering of a dielectric particle in equation (2) yields a specific polarizability of $\frac{\alpha}{m} = 239 \pm 4 \text{ \AA}^3 \text{ kDa}^{-1}$.

Data availability

The raw data and analysed data required to reproduce the figures in the paper are available via the Oxford Research Archive at <https://doi.org/10.5287/ora-exv8qxx5m>.

Code availability

The Python code used for image processing, particle detection and fitting is available via the Oxford Research Archive at <https://doi.org/10.5287/ora-exv8qxx5m>.

References

- Rockward, W. S., Thomas, A. L., Zhao, B. & DiMarzio, C. A. Quantitative phase measurements using optical quadrature microscopy. *Appl. Opt.* **47**, 1684–1696 (2008).
- Thiele, J. C., Pfitzner, E. & Kukura, P. Data from: Single-protein optical holography. *ORA* <https://doi.org/10.5287/ora-exv8qxx5m> (2024).
- Loy, G. & Zelinsky, A. Fast radial symmetry for detecting points of interest. *IEEE Trans. Pattern Anal. Mach. Intell.* **25**, 959–973 (2003).
- Sumlin, B. J., Heinson, W. R. & Chakrabarty, R. K. Retrieving the aerosol complex refractive index using PyMieScatt: a Mie computational package with visualization capabilities. *J. Quant. Spectrosc. Radiat. Transf.* **205**, 127–134 (2018).
- McPeak, K. M. et al. Plasmonic films can easily be better: rules and recipes. *ACS Photonics* **2**, 326–333 (2015).
- Hale, G. M. & Querry, M. R. Optical constants of water in the 200-nm to 200- μm wavelength region. *Appl. Opt.* **12**, 555–563 (1973).
- Seabold, S. & Perktold, J. Statsmodels: econometric and statistical modeling with Python. In *Proc. 9th Python in Science Conference* 92–96 (2010).

Acknowledgements

We thank the Micron Bioimaging Facility of the University of Oxford for loaning a water-immersion objective and J. Becker for fruitful discussions. The protein was supplied by M. Kushwar. E.P. was supported by the Deutsche Forschungsgemeinschaft (DFG, German Research Foundation) under project 455633413. The work was supported by European Research Council (ERC) Consolidator Grant PHOTOMASS 819593 and Engineering and Physical Sciences Research Council (EPSRC) Leadership Fellowship EP/T03419X/1 (P.K./J.C.T.). For the purpose of Open Access, the author has applied a CC BY public copyright licence to any Author Accepted Manuscript (AAM) version arising from this submission.

Author contributions

J.C.T. and E.P. contributed equally to this work. All authors designed the experiments. J.C.T. and E.P. performed the experiments and analysed the data. All authors wrote and finalized the manuscript.

Competing interests

P.K. is a founder, shareholder and non-executive director of Refeyn Ltd.

Additional information

Supplementary information The online version contains supplementary material available at <https://doi.org/10.1038/s41566-024-01405-2>.

Correspondence and requests for materials should be addressed to Philipp Kukura.

reviewer(s) for their contribution to the peer review of this work.

Peer review information *Nature Photonics* thanks Chia-Lung Hsieh, Marek Piliarik and the other, anonymous,

Reprints and permissions information is available at www.nature.com/reprints.